Effect of supersonic fine particle bombardment on microstructure and fatigue properties of Ti-6.5Al-3.5Mo-1.5Zr-0.3Si titanium alloy at different temperatures

Yongli Wu [a], Yi Xiong [a,b,*], Wei Liu [a,b], Zhengge Chen [c], Xin Zhang [a], Shubo Wang [d], Wei Cao [d]

[a] School of Materials Science and Engineering, Henan University of Science and Technology, Luoyang 471023, Henan, China

[b] Collaborative innovation center of new nonferrous metal materials and advanced processing technology jointly established by the Ministry of science and technology, Luoyang 471023, Henan, China

[c] State Key Laboratory of Laser Interaction with Matter, Northwest Institute of Nuclear Technology, Xi'an 710024, Shanxi, China

[d] Nano and Molecular Systems Research Unit, University of Oulu, FIN-90014, Finland

* Corresponding author: Yi Xiong

E-mail address: xiongy@haust.edu.cn

Postal address: School of Materials Science and Engineering, Henan University of Science and Technology, Luoyang 471023, Henan, China

Telephone: +8613526917962

Abstract

In this work, supersonic fine particle bombardment (SFPB) was applied to modify surface of TC11 alloy and its impacts on microstructure and fatigue properties were systematically studied. The modified surface owned a nanoscale grain structure and a compressive residual stress with an amplitude of −196 MPa. The depth of hardened layer was about 300 μm. Afterwards, high-cycle fatigue behavior of SFPB modified alloy at −30 °C, 25 °C and 150 °C was studied, and the fracture surface, microstructure evolution, residual stress relaxation and microhardness of Ti alloy were characterized. The results show that the fatigue strength of the alloy is significantly improved by SFPB, and the fatigue strength decreases with the testing temperature. The deformation induced martensite appears in the subsurface structure of Ti alloy tested at 25 °C and 150 °C, and the amount of deformation-induced martensite increases with the fatigue loading temperature. The compressive residual stress field induced by SFPB is relaxed in different degrees during fatigue loading. The degree of residual stress relaxation is the lowest under fatigue loading at 150 ◦C due to low cycle life. Mechanisms leading to the microstructural evolution and mechanical property variations were also proposed.

Keywords: Supersonic fine particle bombardment; Ti alloy; High-cycle fatigue; Deformation-induced martensite; Stress relaxation.

1. Introduction

T Ti alloys are widely used in the manufacturing of important components, such as blisks in aircraft engines, due to their high strength-to-weight ratio and fatigue strength, excellent corrosion resistance, and wide range of service temperatures [1,2]. In different phases of a flight, these components have to go through a coupling action of temperature changes and high-frequency vibration loading [3]. Under such circumstances, cracks are very easy to turn out on the surface, which then leads to fatigue failures.

Various surface modification technologies have been used to improve the fatigue performances of Ti alloys during the fabrication of engine components. For example, shot peening (SP) has received considerable attentions due to its capability to induced residue stresses by bombarding parts of a surface with small particles. Chen et al. [4] found that the fatigue life of Ti_2AlNb alloy was prolonged by more than 25 times after SP. The extended fatigue life was mainly attributed to the residual stress that hindered the propagation of cracks. Laser or ultrasonic shot peening (LSP or USSP) employs high power intensity laser beams or small particles at ultrasonic frequency. Nie et al. [5] found that multiple LSPs improved the high-cycle fatigue properties of TC11 alloy. When the residual stress was relaxed during multiple LSPs, the surface nanocrystalline structure was the principal factor to improve the high-cycle fatigue properties. Luo et al. [6] reported that after a compound processing of LSP and vibration finishing, the compressive residual stress of Ti-3.5Mo-6.5Al-1.5Zr-0.25Si was larger and the surface nanocrystalline structure was more uniform than that of single LSP. This enhanced surface integrity led to 106 MPa increase of fatigue strength. The fatigue life of Ti-6Al-4V gained 4 times after USSP as reported by Kumar et al. [7]. The increase of fatigue life was correlated to residual stress, work hardening and grain refinement in the

surface area.

In addition to aforementioned techniques, supersonic fine particle bombardment of (SFPB) has recently emerged as a novel surface modification technology. During SFPB, the metal surface is repeatedly bombarded by numerous fine solid particles with a diameter of 0.05–200 μm carried by supersonically compressed air at rates between 300 and 1200 m/s. This process is proposed to be a promising alternative to conventional SPs because of higher depth of residue stresses into the surface, better surface finishing, higher efficiency of surface nanocrystallization, and meanwhile simple and convenient operations [8]. Additionally, SFPB is a more versatile process and capable of handling components with large sizes and complex shapes [9,10]. Therefore, it is more suitable for industrial productions compared to the SP. Up to now, SFPB has been successfully applied to alloys such as steel [11], Cu alloys [12], Al alloys [13], and Ti alloy [14]. However, investigations on Ti alloys processed by SFPB are mainly focused on the mechanisms of surface nanocrystallization and the surface's thermal stability, tribological performance and corrosion resistance [14–18]. Knowledge remains unclear for the microstructural evolution of the deformed surface, especially the subsurface layer where is generally believed to be the fatigue initiatives after surface modifications. Thus, it is important to study the microstructure in the subsurface layer before/after fatigue loading to reveal the influence of SFPB on the fatigue performance of Ti alloys.

In this work, we presented a systematic study of microstructural evolution and fatigue properties of a TC11 alloy treated by SFPB. This Ti alloy is selected due to its high strength, excellent creep resistance and thermal stability but meanwhile sensitiveness to surface defects [19]. The high cycle fatigue tests were carried out at three typical temperatures of −30 ˚C, 25 ˚C, and 150 ˚C, corresponding to these during aircraft services. The microstructure evolution

of subsurface layer after fatigue was explored to reveal the fatigue failure mechanisms. This work is aimed to serve an experimental basis and technical support for advanced anti-fatigue manufacturing of Ti alloy-based aviation components, and to achieve the goal of "lightweight, long life, high stability and reliability" of Ti alloy components.

2. Experimental

The material used in the experiment was a commercial TC11 alloy in the form of cold-rolled sheets from Chengjin Titanium Industry Co., Ltd (Baoji, China). The nominal chemical composition of this alloy was shown in Table 1.

Table 1 Nominal chemical composition of TC11 alloy (wt%)

Al	Mo	Zr	Si	Ti
6.50	3.50	1.50	0.30	Bal.

Before SFPB, the TC11 alloy sheet with a size of 300 mm × 200 mm × 37 mm was duplexily annealed in a vacuum furnace protected by Ar gas to obtain a lamellar structure. The duplex annealing was carried out as follows: isothermal holding at 970 ℃ for 1.5 h firstly, air cooling to 530 ℃ and holding for 6 h, and finally air cooling to room temperature. The obtained lamellar structure had a microhardness of 336 Hv, ultimate tensile strength of 1083 MPa, yield strength of 982 MPa, and elongation of 12.86%, respectively. The annealed TC11 alloy then was machined into the high-cycle fatigue samples whose geometry is shown in Fgi. 1. Then SFPB surface modification was performed on both sides of the gauge (red shaded) section.

The SFPB surface modifications were carried out using an equipment made by Shenyang Institute of Metals, Chinese Academy of Sciences. More details about the instrumentation of

SFPB can be found in [20]. During SFPB, the applied pressure of compressed gas was 1.2 MPa and the spray angle was 85°, as optimized in our previous work [21]. The distance between the nozzle and the sample was 40 mm. The impact particles were spherical Al_2O_3 with Mohs hardness of 8 and average size of ~50 μm (Fig. 22). The particle velocity was 450~550 m/s, the gas flow rate was 10~30 g/s, and the impact time was 90 s. After SFPB, the surface roughness was measured by a SuperViewW1 optical 3D surface profiler.

High-cycle fatigue tests of the modified TC11 alloys were carried out at -30 ℃, 25 ℃, and 150 ℃ on a QBG-50 fatigue tester with a stress ratio r = 0.1 and a loading frequency of 25 Hz. An environment box was used to maintain the testing temperatures of -30 ℃ and 150 ℃. The samples used for detailed microstructure evolution, residual stress, microhardness, fatigue fractures were fatigued under an applied stress amplitude σa of 500 MPa and sectioned via a wire-electrode cutting method. A JSM-7900F field emission scanning electron microscope was used for the fatigue fractures and cross-sectional morphology characterization. Thin foils for transmission electron microscope (TEM) were prepared using the Gatan 691 ion milling and characterized by using a JEM-2010 TEM operated at 200 kV. XRD patterns of the TC11 alloys were acquired using a D8 ADVANCE X-ray diffractometer with monochromated CuKα radiation. The scan angle ranged from 30° to 90° with a step of 0.02° and a scan speed of 2°/min. The voltage was 40 kV and the current was 40 mA. The surface residual stress of the SFPB treated specimen was measured by an X-350A X-ray stress analyzer with CuKα radiation. The diffraction crystal plane was the {213} planes of α phase. The voltage and the current were 27 kV and 7 mA, respectively. The tube diameter was 4 mm and the heeling angle was selected as 0°, 15°, 30°, 45°. The surface obtained residual stress was an average of three measurements at different positions located at 9 mm from the fracture

surface (edge of the modified area). Microhardness measurements were performed using a MH-3 microhardness tester on cross section of the specimens. The load force is 200 gf with a dwelling time of 10 s. The hardness value was the average of at least five measured points at the same depth.

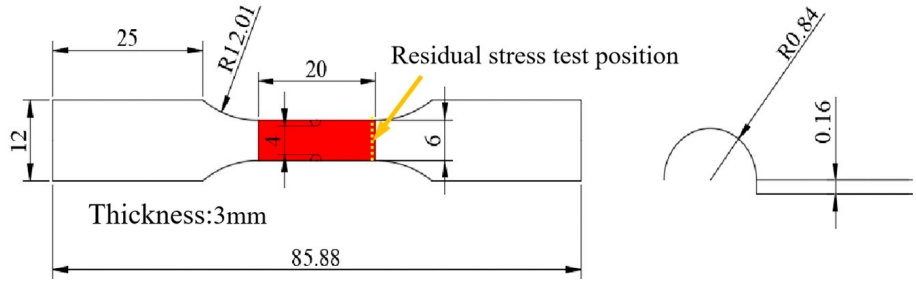

Fig. 1 Schematic drawing of the sample employed in the fatigue tests. The red shaded area represents the SFPB modified area on double sides of the fatigue samples. All dimensions are given in mm.

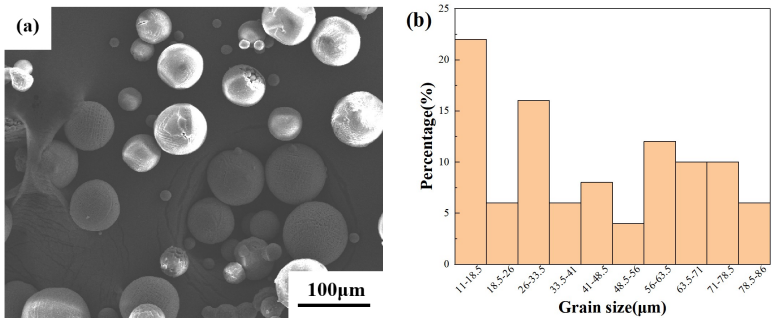

Fig. 2 Al_2O_3 particles used for SFPB: (a) SEM image and (b) particle size distribution histogram.

3. Results and discussions

3.1 Surface and subsurface properties and microstructures before fatigue loading

The surface finishing, represented by surface roughness of the TC11 alloy before and after SFPB, is shown in Fig. 3. The alloy surface without SFPB was relatively flat. Scratches with regular intervals due to mechanical grinding were observed (Fig. 3(a)). The surface roughness (Sa) and peak-to-valley value (PV) is estimated to be 0.564 μm and 4.596 μm,

147 respectively. After SFPB, Sa and PV increased significantly to 5.531 μm and 17.791 μm,
148 respectively (Fig. 3(b)). This is due to the large number of microdents induced directly by
149 impacting the alloy surface with high-energy and high-speed Al_2O_3 projectiles (Fig. 4(a)).
150 Nevertheless, this surface finishing by SFPB is much better compared to conventional SP [10].
151 The surface finishing, represented by surface roughness of the TC11 alloy before and after
152 SFPB, is shown in Fig. 3. The alloy surface without SFPB was relatively flat. Scratches with
153 regular intervals due to mechanical grinding were observed (Fig. 3a). The surface roughness
154 (Sa) and peak-to-valley value (PV) is estimated to be 0.564 μm and 4.596 μm, respectively.
155 After SFPB, Sa and PV increased significantly to 5.531 μm and 17.791 μm, respectively (Fig.
156 3b). This is due to the large number of microdents induced directly by impacting the alloy
157 surface with high-energy and high-speed Al_2O_3 projectiles (Fig. 4a). Nevertheless, this surface
158 finishing by SFPB is much better compared to conventional SP [10].

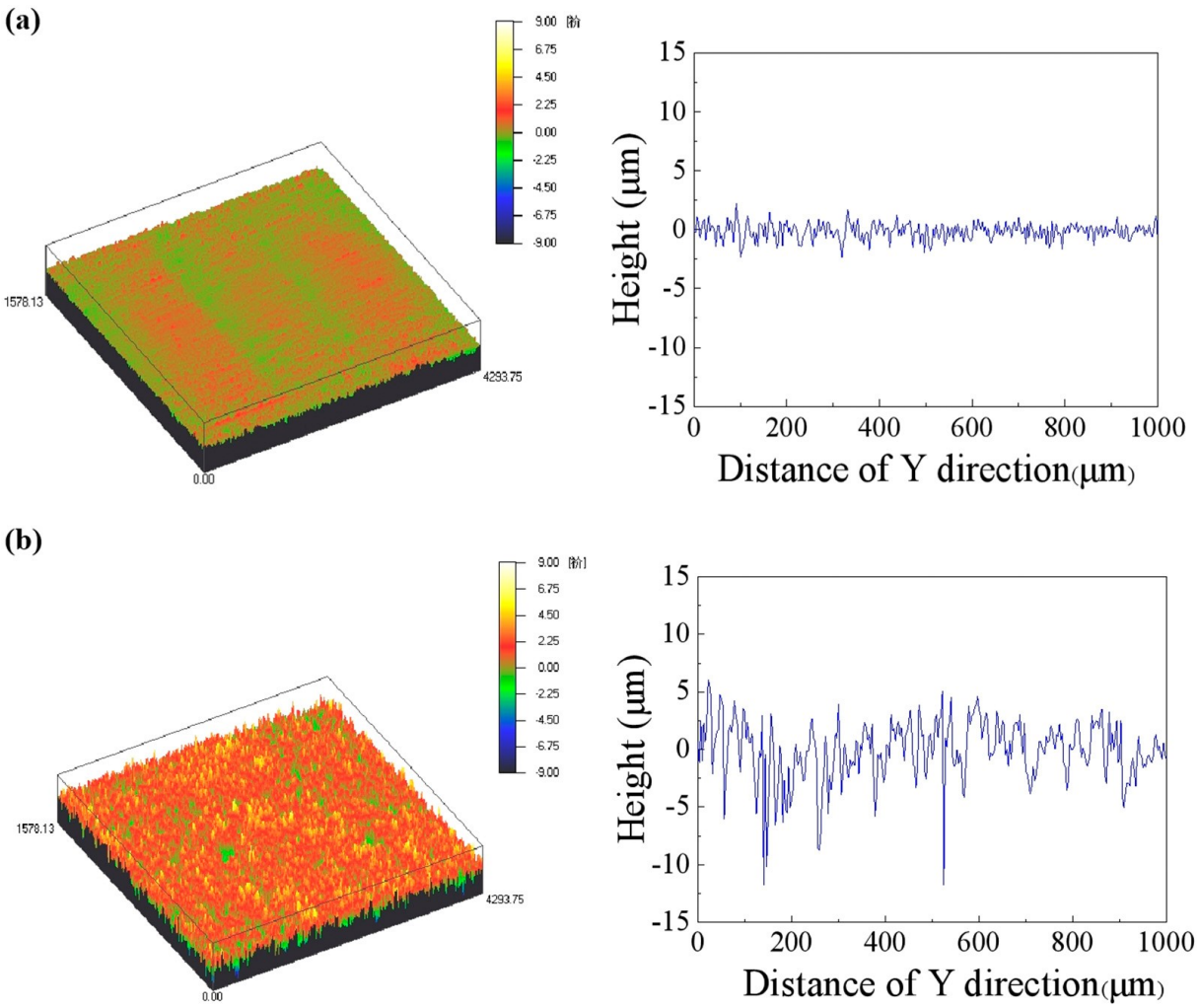

Fig. 3 Three-dimensional morphology and surface roughness of TC11 alloy (a) before and (b) after SFPB.

Fig. 4(a) depicts a cross-sectional SEM image of the SFPB modified TC11 alloy before fatigue loading. The α (darker) laths were separated by β laths (brighter) in the bulk that were not affected by SFPB. Microdents on the surface and the severe plastic deformation (SPD) layer with a "rheological layered structure" were seen. This is due to the repetitive high-speed impact of Al_2O_3 particles with high kinetic energy on the alloy surface, generating an equivalent mechanical force. Thus, the surface underwent severe deformation to accommodate the force. The depth of SPD layer was about 30 μm. The inter-lath spacing became smaller and the boundaries were almost indistinguishable in the SPD layer. Meanwhile, the β laths were kinked and bent due to severer local deformation [22]. With

increasing distance from the surface, the inter-lath spacing increased gradually until becoming the same as that of the initial structure. This is related to the degree of plastic deformation, where the farther distance from the surface leads to weaker plastic deformation and wider inter-lath spacing.

TEM observations were conducted to get a better understanding of the microstructure evolution after SFPB. Fig. 4(b-c) shows the TEM images of the uppermost surface, in which a large number of dislocations were observed to accumulate and develop into dense dislocation walls and cells. The initial coarse lamellae disappeared and were severely refined, which is ascribed to formation of (sub)grains through the development of various dislocation structures during SFPB [23]. In the selected area electron diffraction (SAED) pattern (inset of Fig. 4(b)), a continuous ring confirms that the grain structure has been refined to nanoscale and the grains have a relatively random orientation distribution [24]. The average grain size was about 10.3 nm as estimated through the Nano Measurer software [25] from the TEM images (inset of Fig. 4(c)).

Fig. 4(d) shows a TEM image taken from the subsurface layer, about 100 μm from the surface. Deformation twins and a large amount of dislocation tangles presented in α laths. This is mainly due to that the development of deformation twins is necessary for the hexagonal close packed (hcp) α phase with low stacking fault energy (SFE) to maintain the plastic deformation compatibility. On the other hand, body-centered cubic (bcc) β phase has higher SFE and more active slip systems, in which dislocation migration is easier during plastic deformation. Nevertheless, due to the different crystallographic structures and orientations between α and β phases, dislocation slip directions in α are different from that in neighbouring β. Thus, the phase boundaries can have a strong pinning effect on mobile

dislocations. It leads to the pile-up and accumulation of high-density dislocations to form the dislocation walls at the phase boundaries which are sensitive to stress concentration and the crack initiation during fatigue cycling [26].

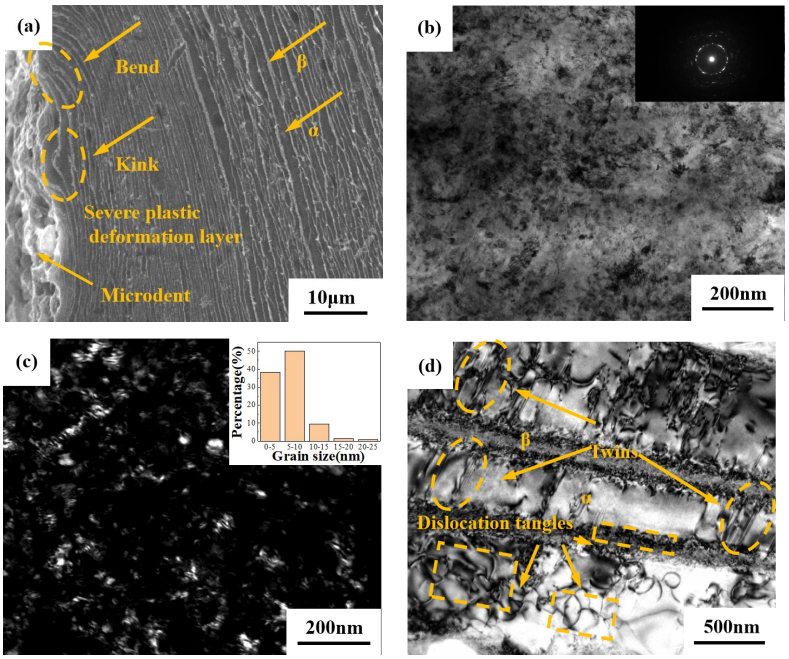

Fig. 4 Microstructure of the SFPB modified TC11 alloy before fatigue loading: (a) SEM image of the cross section; (b) TEM bright-field (BF), and (c) dark-field (DF) image of the uppermost surface; (d) TEM BF image of the subsurface layer (100 μm from the uppermost surface). Inset of (b) shows the SAED pattern, and inset of (c) presents the grain size distribution histogram calculated by Nano Measurer software.

3.2 Fatigue behaviors and fracture surfaces

The stress-life (S–N) curves of TC11 alloys at different temperatures with and without SFPB are presented in Fig. 5. There was an increase by 13%, 11.1%, 6.6% at 10^7 cycles at −30 ˚C, 25 ˚C, and 150 ˚C, i.e. an increase in the endurance strength by 60 MPa, 50 MPa, 25 MPa with SFPB, respectively. Thus, it can be concluded that the fatigue life of TC11 alloy can be enhanced by SFPB surface modification despite of the increased roughness (Fig. 3). The rougher surfaces might result in easier stress concentration as crack sources. Nevertheless,

this possible detrimental effect on fatigue strength can still be compensated by gradient nanostructures (Fig. 4) and related residual stresses (Fig. 9), work hardening induced by SFPB. The nanostructures formed at the SFPB modified surface can help to disperse the stress concentration and effectively inhibit nucleation of cracks [27]. The residual compressive stress field with an amplitude of −196 MPa at the surface balances the tensile stresses generated under cyclic to prevent crack propagation and even close the cracks [28]. The significant increase in surface micro- hardness of SFPB modified TC11 alloy (Fig. 10) also indicates the in- crease in resistance to fatigue as well as in surface strength. The fatigue life of the alloy, thus, is prolonged after SFPB surface modification.

However, the fatigue strength of TC11 alloys decreases with increasing fatigue testing temperature, an increase by 5%, 31% for 10^7 cycles at −30 ˚C comparing with that at 25 ˚C and 150 ˚C. This result associates with the different mobility of dislocations at different temperatures [29] which led to different evolution behavior of residual stress, microhardness and microstructure during fatigue loading.

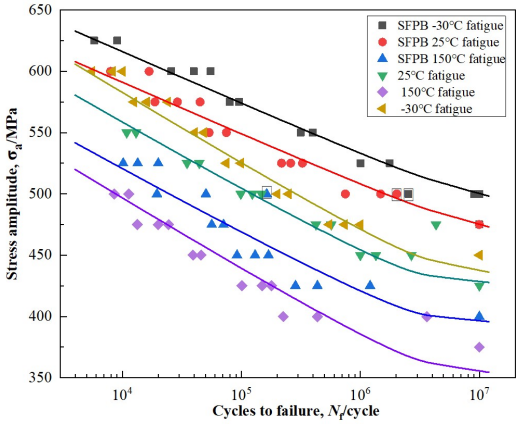

Fig. 5 Stress-life (S-N) curves of TC11 alloys fatigued at different temperatures.

Fig. 6 shows the fracture surfaces of TC11 alloys after fatigue failure under a stress amplitude σ_a of 500 MPa. At these three temperatures, macroscopic views of the fracture surfaces represent mechanical fatigue fracture features in Fig. 6(a-c). These fracture surfaces

were generally characterized by three different regions, fatigue source zone (I), crack propagation zone (II) and transient fracture zone (III). It is noticed that the radial edges extended from the zone I to the zone II, resulting in relatively flat fracture surfaces. From the magnified views of zone I (Fig. 6(aI-cI)), the crack initiation site, as indicated by the dashed ellipses of the SFPB modified TC11 alloy, was observed to locate in the subsurface layers. The depth of these fatigue sources is measured to be 117 μm, 98 μm and 39 μm at −30 ˚C, 25 ˚C, and 150 ˚C, respectively. These results have demonstrated that the fatigue source moves to the subsurface layer after SFPB. However, the crack initiation site still gradually moved to the surface with increasing temperature, indicating that the retarding effect of SFPB on crack initiation has been weakened at high temperatures. Fatigue life is essentially related to the sites for crack initiation [7]. The much smaller depth explains why the fatigue life of TC11 alloy was the shortest at 150 ˚C.

With the increase of fatigue cycling numbers, the crack began to propagate radially around the fatigue source after reaching the critical stress for crack propagation, forming zone II (Fig. 6(aII-cII)). A river-like pattern and fatigue striations were seen on SEM images of samples treated at all three temperatures. These fatigue striations, representing the propagation trace of stress cycle, were parallel to each other but perpendicular to the crack propagation direction. The width of fatigue striation d is defined as:

$$d = D/(n-1) \qquad \text{Eq. 1}$$

where D is the summed widths of the first to the n_{th} fatigue striation [30]. The d is calculated to 0.6 μm, 0.67 μm and 0.8 μm at -30 ℃, 25 ℃ and 150 ℃, respectively. The magnitude of d is believed to be related to the interaction between the crack tip and dislocations [31]. At 150 ℃, more slip systems can be activated and weakened the interaction between crack tip

and dislocation, resulting in a reduction of energy consumption. Consequently, the *d* and crack growth rate increased with increasing temperatures. Therefore, zone II is larger at -30 ℃ than that at 25 ℃ and 150 ℃. Nevertheless, the number of secondary cracks was observed to increase, and the propagation path of the main crack became more tortuous with increasing temperatures. This phenomenon may be related to the temperature-dependent deformation-induced martensitic transformation (Fig. 12(e-f)).

When the crack propagated to a critical size, the specimen fractured, thus forming zone III (Fig. 6(aIII-cIII)). There were a large number of dimples in this zone. At -30 ℃ (Fig. 6(aIII)), the dimple size was small and uniform. When the temperature rose (Fig. 6(b, cIII)), the dimple size clearly increased and the number decreased, indicating improved ductility.

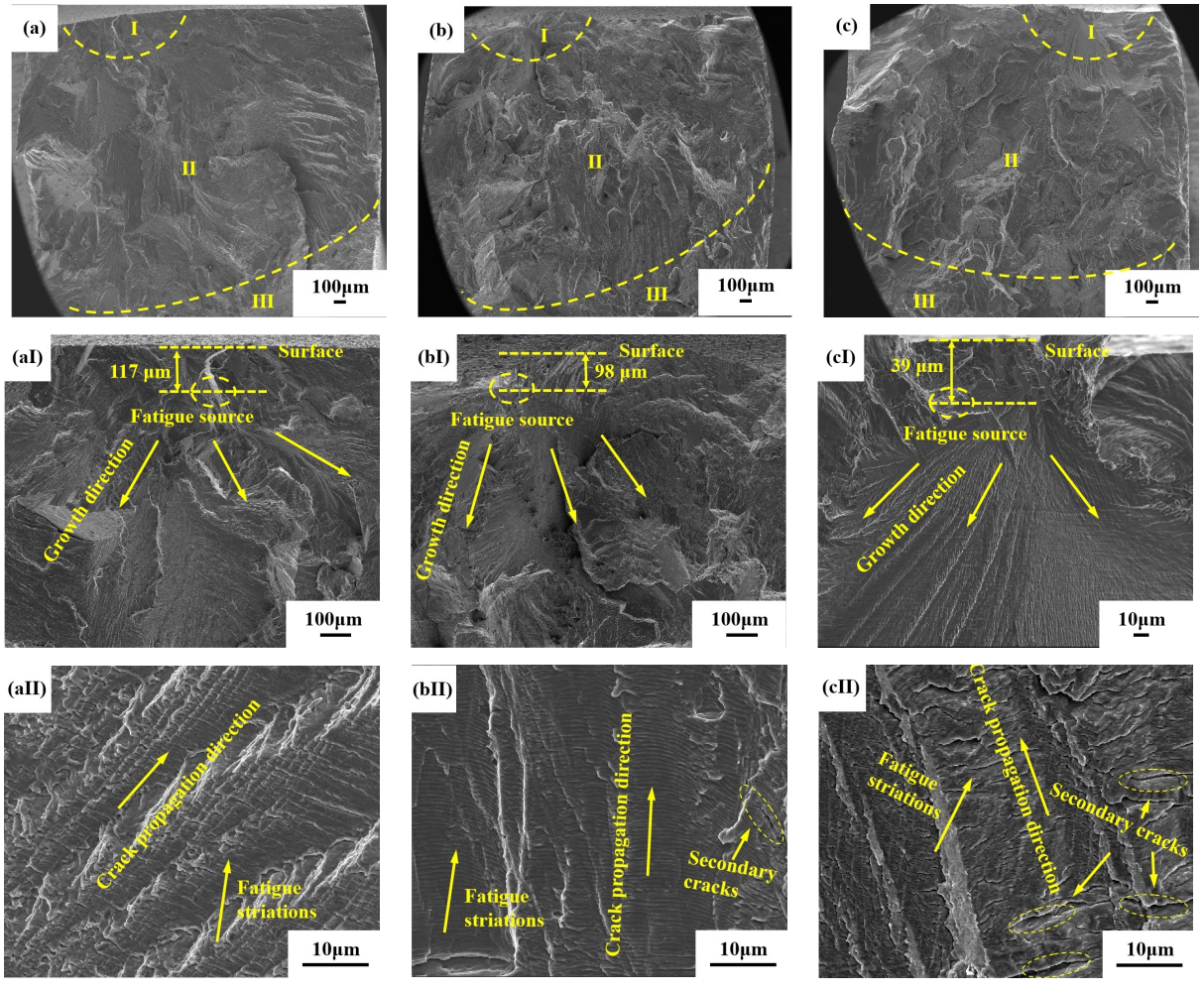

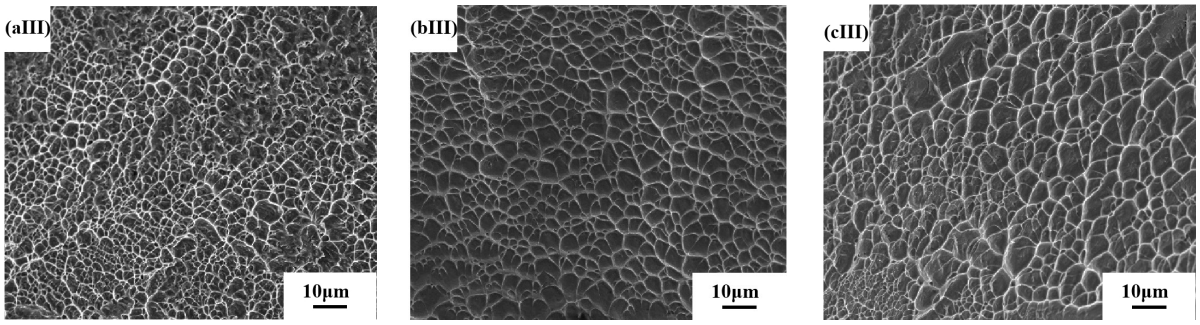

Fig. 6 SEM micrographs of the fracture surfaces of SFPB modified TC11 alloys under a maximum applied stress σ of 500 MPa: macroscopic view of the fracture surfaces at (a) -30 ℃, N = 2 538 700, (b) 25 ℃, N = 2 025 600 and (c) 150 ℃, N = 163 200, respectively. (aI-III, bI-III), and (cI-III) are the higher magnification images of corresponding zones marked in a, b and c, respectively.

3.4 Surface properties after fatigue

Fig. 7 shows the XRD patterns of the uppermost surface of TC11 alloys. No new diffraction peak emerged in the XRD patterns after SFPB treatment. However, all peaks shifted slightly (Fig. 7(a)), suggesting lattice distortion after SFPB. The full width at half maximum (FWHM) of the diffraction peak increased obviously (Fig. 7(b)). This is mainly due to the grain refinement (Fig. 4) and the increase of surface microstrain after SFPB. Furthermore, there was no new diffraction peak after fatigue failure.

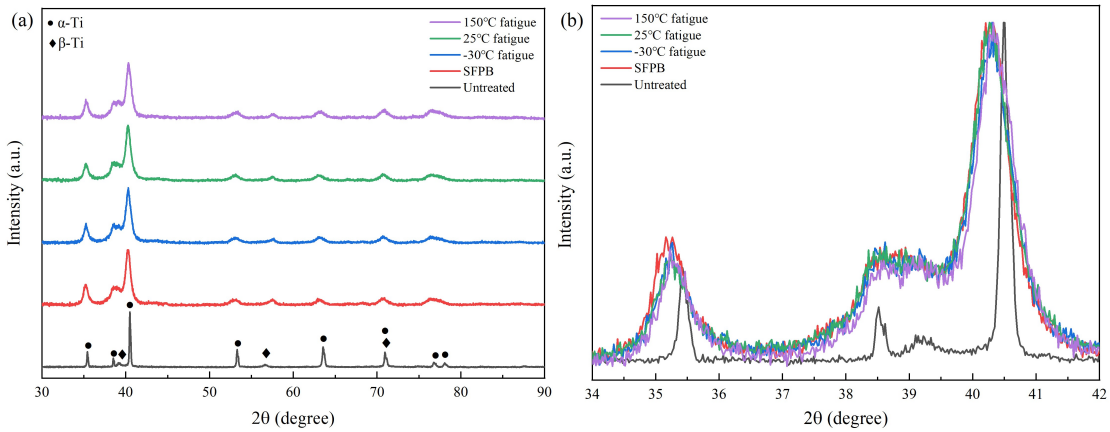

Fig. 7 XRD patterns acquired at the uppermost surface of TC11 alloys: (a) an overview with 2 theta range of 30-90°, and (b) magnified view with 2 theta range of 34-42°. The intensity

has been normalized for better readability.

The Williamson-Hall (W–H) method [32] was used to estimate the microstrain of α and β phase of TC11 alloys after fatigue loading. As shown in Fig. 8, the microstrains of α and β phase increased by 3.33 times and 1.33 times after SFPB, respectively. Nevertheless, the microstrain of α and β phase decreased by 34.9%/51.8%, 33.6%/47.3% and 26.2%/7.1% after fatigue failure at −30 ˚C, 25 ˚C and 150 ˚C, respectively. Residual stress relaxation thus occurred during the fatigue cyclic loading. At a σ_a of 500 MPa, the fatigue cycles were 2,538,700, 2,025,600 and 163,200 cycles for cases of −30 ˚C, 25 ˚C and 150 ˚C, respectively. This low fatigue cycles at 150 ˚C, *i.e.,* much less fatigue times, might lead to the observed high microstrain. Additionally, this relatively high microstrain might also relate with the deformation induced bcc β to α" martensite transformation, which will be further discussed in Section 3.5.

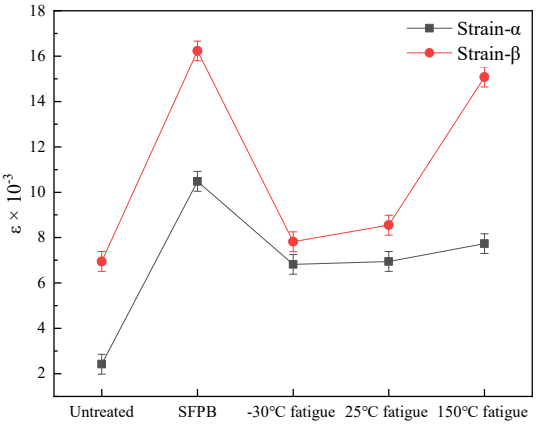

Fig. 8 Microstrain of α and β phase in TC11 alloys after fatigue loading at different temperatures.

Fig. 9 shows the surface residual stress of the SFPB treated TC11 alloys after fatigue loading. During SFPB, lattice distortion occurred, and part of the deformation energy was stored in the form of dislocations. Meanwhile, the formation of subgrains reduced the energy

of the system and increased the bonding force between grains, which produced a compressive residual stress of −196 MPa. After fatigue failure at −30 ˚C, 25 ˚C, and 150 ˚C, the compressive residual stresses of the surfaces relaxed to −99 MPa, −125 MPa, and −175 MPa, respectively. During cyclic loading, the stored dislocations rearranged, leading to dynamic recovery and stress relaxation. Because residual stress relaxes at each cycle, the degree of residual stress relaxation is closely related to the fatigue cycle numbers [33]. As shown in Fig. 5, the fatigue cycle lives at −30 ˚C and 25 ˚C are significantly higher than that at 150 ˚C. Hence, the residual stress relaxation level is the largest, about 50% at −30 ˚C. At 150 ˚C, the degree of residual stress relaxation, about 10%, is the smallest following its fatigue life. This result is in good agreement with the XRD microstrain analysis. Additionally, the relatively high micro- strain and weak residual stress relaxation might also be related with the deformation induced bcc β to martensite α" transformation. This will be further discussed in a later section of 3.5.

The dependence of microhardness on depth distribution of TC11 alloy after fatigue loading is visualized in Fig. 10. The microhardness achieves its maximal, 445 HV, at the surface after SFPB, then decreases to the bulk hardness, about 320 HV, towards interior. The depth of hardened layer by SFPB is about 300 μm. This behavior is consistent with those after SP [34] and USRP [28], and is attributed to the gradient microstructures and work hardening by the surface modifications. The hardness distribution along depth after fatigue loading at different temperatures followed a similar trend as that without fatigue, but the corresponding hardness values at the same depth were lower and decreased with the operation temperature. The maximum hardness values are 437 HV, 392 HV and 381 HV at the alloy surface after fatigue failure at −30 ˚C, 25 ˚C and 150 ˚C, respectively. Meanwhile, at the subsurface layer,

the hardness values after fatigue failure at 150 ˚C were comparable with those at 25 ˚C at the range of more than 60 μm from the surface. It suggests that the residual tress relaxation probably take places mainly at the surface during fatigue at 150 ˚C.

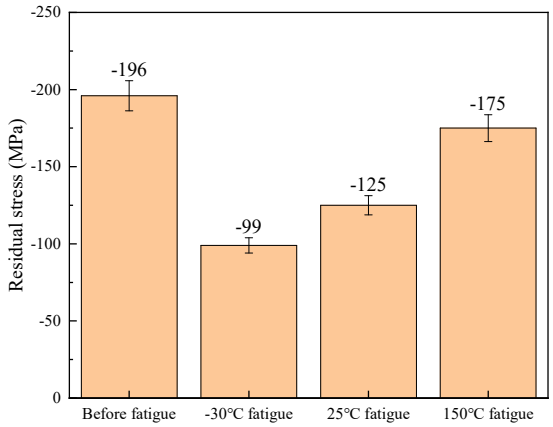

Fig. 9 Surface residual stress of the SFPB modified TC11 alloys after fatigue failure at different temperatures.

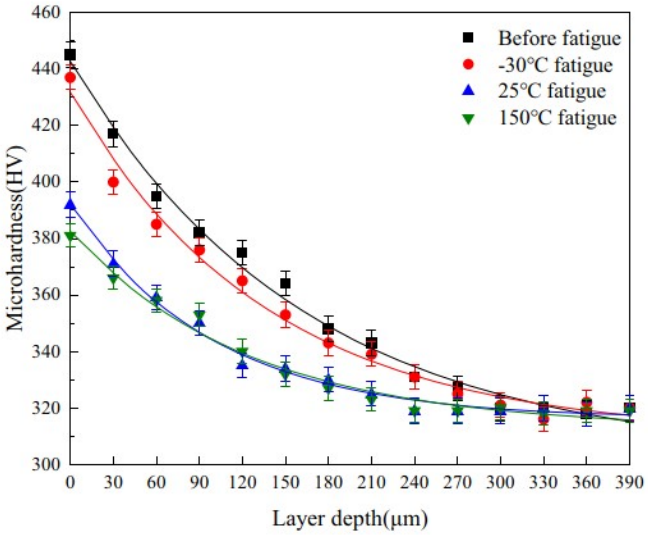

Fig. 10 Microhardness vs depth distribution in SFPB modified TC11 alloy after fatigue loading at different temperatures.

3.5 Surface after fatigue failure

TEM observations at the surface of SFPB modified TC11 alloy after fatigue faliure at different temperatures are shown in Fig. 11. Continuous rings were found in the SAED

patterns in Fig. 11(a, c, e), indicating that the grains remained at nanoscale and randomly oriented after failure. The average grain size at -30 °C (Fig. 11(b) is estimated to ~10.5 nm, almost the same as that before fatigue loading (Fig. 4(c)). With increasing fatigue temperatures to 25 and 150 °C, the average grain size increases to 11.3 and 12.4 nm, respectively. This is mainly due to accelerated recovery in the SPD surface layer at elevated temperatures.

The strength of a material can be calculated by [35]:

$$\sigma_f = \sigma_0 + k(d_{fp})^{-1/2} + \alpha G b \rho^{1/2} \quad \text{Eq. 2}$$

where σ_f is the strength, σ_0 the friction stress, k the Hall-Petch constant, d_{fp} the dislocation mean free path, G the shear modulus, b the Burgers vector and ρ the dislocation density. From the equation, it can be seen that an increase of ρ and a decrease of d_{fp} can increase the strength and hardness of the material.-The TEM-BF images (Fig. 11) show that the dislocation density decreased as the temperature increased. The alloy surface grains were the finest, meaning that the d_{fp} was the lowest during fatigue at -30 ℃. Generally, there is a positive correlation between the strength and fatigue strength [36]. Thus, the TC11 alloy exhibited best fatigue performance, longest fatigue life and highest hardness at -30 ℃.

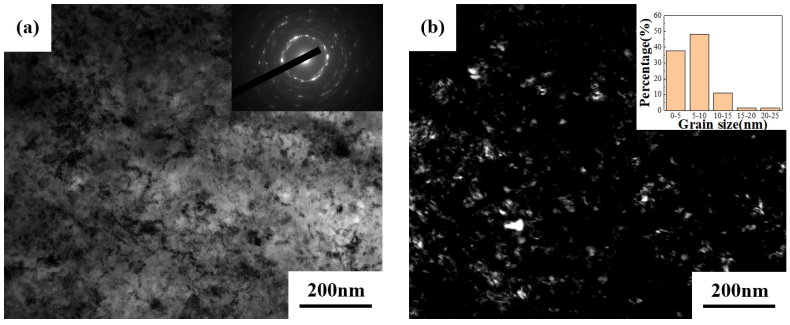

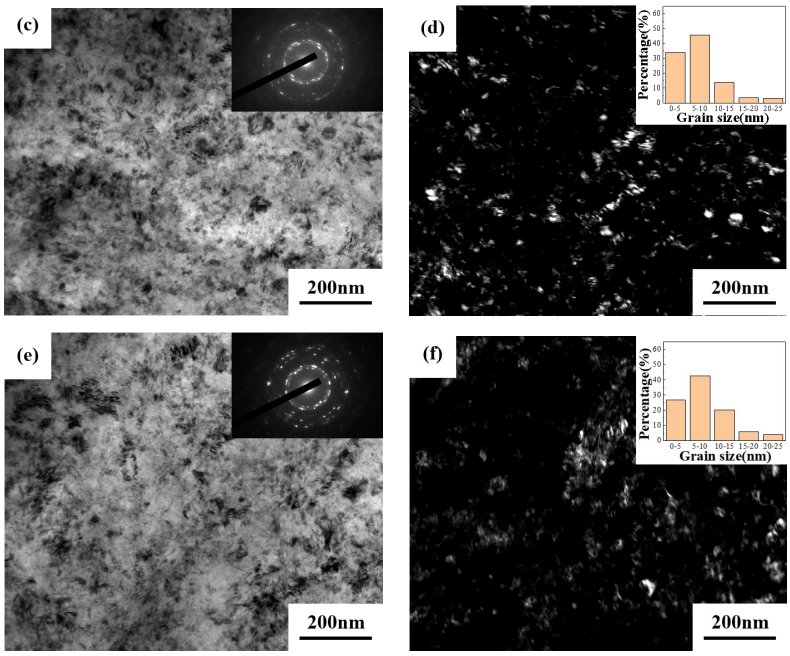

Fig. 11 TEM images of the surfaces of SFPB modified TC11 alloy after fatigue failure. (a, c, e) BF image at -30 °C, 25 °C, 150 °C; (b, d, f) DF image at -30 °C, 25 °C, 150 °C, respectively. Inset of (a, c, e) shows the SAED pattern, and inset of (b, d, f) presents the grain size distribution calculated by Nano Measurer software.

3.6 Subsurface after fatigue loading

To reveal the influence of subsurface microstructure on fatigue behavior, the microstructure evolution of the alloy subsurface layer after fatigue failure was studied via TEM observations. Comparing with the microstructure before fatigue loading (Fig. 4), more deformation twins (Fig. 12(a)) and higher density stacking faults (Fig. 12(b)) were seen in α lamellar matrix after fatigue failure at -30 °C. In addition, there are high-density dislocations in α and β lamellae, and most of them accumulate at the interface between α and β. At 25 °C, there are a large number of dislocation tangles in β and the dislocation wall formed by orderly arrangement of dislocations at the interface of α and β (Fig. 12 (c)). Some stacking faults were also produced in α lamellae. Dendritic phases distributed discontinuously between β lamellae

were observed in Fig. 12(d), which are determined as the deformation-induced martensite α" according to the indexing of SAED pattern (Fig. 12 (e)). This α" was not detected in the XRD pattern (Fig. 7), which might be due to that the α" content was relatively low and difficult to distinguish, or that the X-ray penetration depth is too small to characterize the α" at the subsurface layer. Large amounts of dislocation tangles were found in β of the 150 °C treated samples (Fig. 12(f)). More α" were formed and surrounded by dislocation tangles (Fig. 12 (g)). These α" martensite have a twin structure with twin planes of {111} (Fig. 12 (h)).

The above results revealed that TC11 alloy coordinated deformation by producing a large number of deformation twins, stacking faults, dislocation tangles in α phase and dislocation tangles in β phase at -30 ℃. While at 25 ℃, the alloy coordinated deformation mainly by producing a small amount of stacking faults in α phase and a large amount of dislocation tangles in β phase and a small amount of deformation-induced martensite. When the temperature increases to 150 ℃, the main deformation mechanism changes to deformation-induced martensitic transformation in β phase. The emergence of deformation twins and stacking faults was related to the significantly reduced SFE with alloying element Al at lower temperatures [37,38]. The lowered SFE leads to low activation energy for twin formation and low mobility of dislocations. Thus, many twins and stacking faults were observed at -30 ℃. Twin boundaries are similar to the grain boundaries, which not only hinder dislocation slip, but also provide nucleation sites for dislocations [39]. The generation and interactions between such a large number of defects such as dislocation tangles, twins and stacking faults significantly improve the fatigue performance of TC11 alloy at -30 ℃.

The appearance of deformation-induced martensite at 25 ℃ is related to the stability of β phase that is closely associated with the chemical composition of the alloy [40]. According to

[41], the deformation-induced martensite transformation temperature varies with the stability coefficient, K_β, of β phase. In the TC11 alloy, the K_β value was calculated to be 0.35, meaning that the deformation-induced martensitic transformation temperature should be above room temperature. After SFPB, many defects were introduced into the TC11 alloy, which led to a sharp increase in energy and the alloy was metastable. The stress concentration at the interfaces between α and β caused by the high-density dislocations (such as Fig. 4(d)), provided the driving force for the nucleation and growth of martensite. As a result, the deformation-induced α" nucleate preferentially at the phase interfaces. Then the martensite grows gradually through the boundary into the α atrix during continuous cyclic loading. As highlighted by the red box in Fig. 13(e), the two α" martensite nucleated at adjacent α and β interfaces grew into the same α lamellar and finally met. When the residual β are transformed to α", the β will be mechanically stabilized. This process hardens β phase and makes the martensitic transformation more difficult [42]. As a result, there was only a small amount of α" at 25 ˚C. The appearance of α" increased the local strength thus prolonged the fatigue life. Meanwhile, the residual compressive stress field is formed at the crack tip, due to volume expansion of the transformation from β to α" [43]. This weakens the relaxation of compressive residual stress and increases the stress intensity factor threshold. At 150 ˚C, the β phase softened, facilitating the deformation-induced martensitic trans- formation. Hence, there was larger amount of α" after being tested at 150 ˚C compared with the one at 25 ˚C. It might suppress the progress of stress relaxation and contribute to the lowest degree of residual stress relaxation to a certain extent at 150 ˚C.

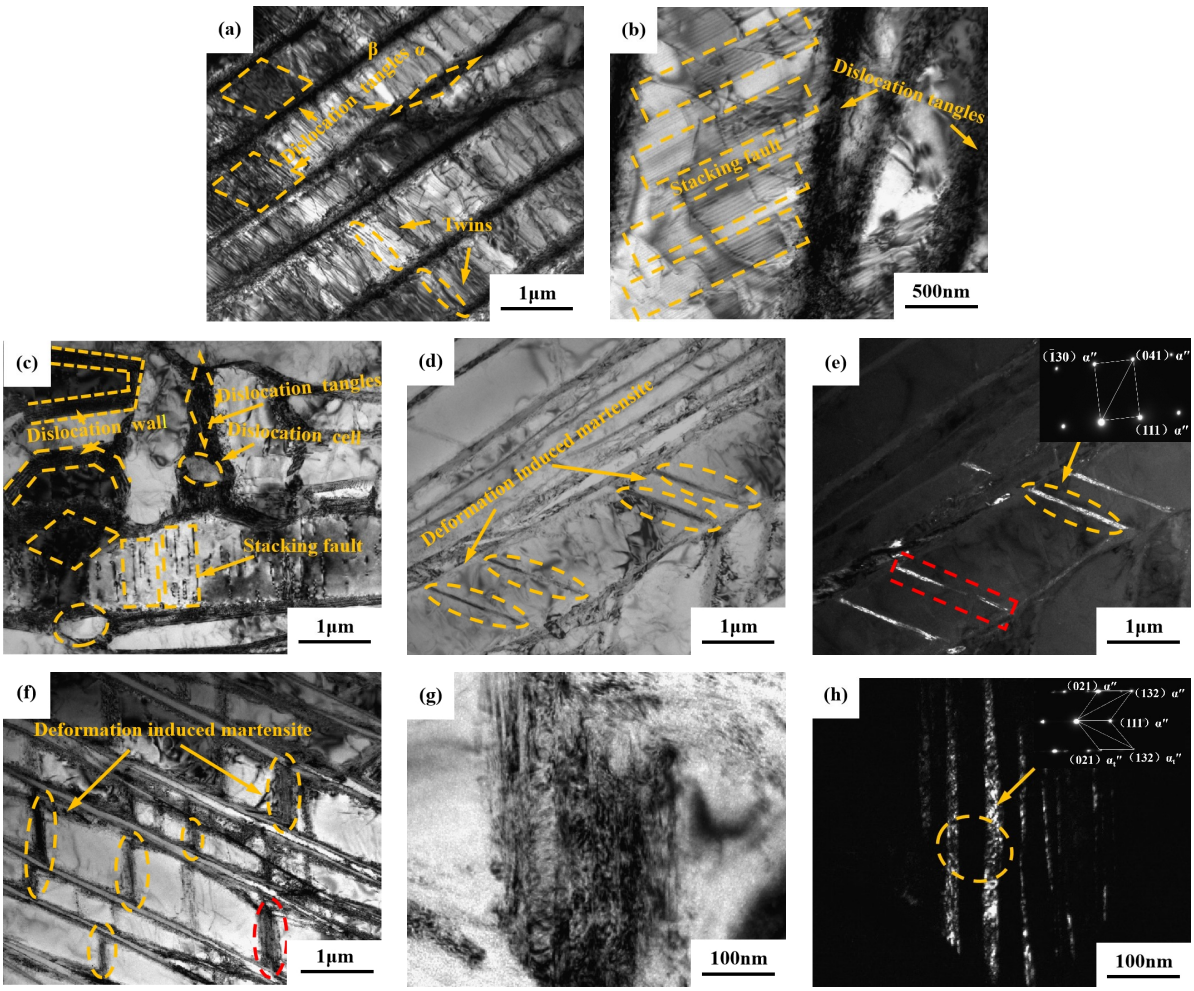

Fig. 12 TEM images of the subsurface (100 μm from the surface) of the SFPB treated TC11 alloy after fatigue loading at different temperatures: (a,b) at -30 °C; (c, d) at 25 °C; (e) DF image and corresponding SAED pattern of (d); (f) at 150 °C; (g) the magnification of the red elliptical region of f; (h) DF image and corresponding SAED pattern of (g).

4. Conclusion

In this study, the influence of SFPB on the fatigue performance of TC11 alloy was investigated. The fatigue tests were performed at different temperatures. By using residual stress measurement, post-mortem SEM and TEM characterizations, the following conclusion can be drawn:

1. The fatigue performance of TC11 alloy after SFPB modification was significant enhanced as compared to that without SFPB. It is due to the nanocrystallization,

residual stresses at the surface introduced by SFPB.

2. The enhancement of fatigue performance of Ti alloy decreased with increasing fatigue test temperature.
3. At -30 ℃, the fatigue deformation of the TC11 alloy was coordinated by a large amount of deformation twins, stacking faults, dislocation tangles in α phase and a large number of dislocations in β phase. As the temperature increases to 25 ℃, the fatigue deformation was coordinated by a small amount of stacking faults in α phase, and numerous dislocation tangles, as well as a small amount of deformation-induced martensite in β phase. Further increasing the temperature to 150 ℃, the main mechanism changed to deformation-induced martensitic transformation in β phase.

CRediT authorship contribution statement

Yongli Wu: Conceptualization, Investigation, Formal analysis, Data Curation, Writing-Original draft, Writing- Reviewing and Editing, Visualization. **Yi Xiong:** Conceptualization, Methodology, Validation, Formal analysis, Investigation, Resources, Writing, Reviewing and Editing, Visualization, Supervision, Project administration, Funding acquisition, Corresponding author during submitting and revision. **Wei Liu:** Formal analysis, Investigation, Data Curation, Writing Reviewing and Editing. **Zhengge Chen:** Software, Validation, Investigation, Resources. **Xin Zhang:** Software, Investigation, Data Curation. **Shubo Wang:** Formal analysis, Software, Validation, Writing, Reviewing and Editing. **Wei Cao:** Conceptualization, Methodology, Formal analysis, Resources, Writing, Review and Editing, Funding acquisition.

Declaration of competing interest

We declare that we have no financial and personal relationships with other people or

organizations that can inappropriately influence our work, there is no professional or other personal interest of any nature or kind in any product, service and/or company that could be construed as influencing the position presented in, or the review of, the manuscript entitled.

Acknowledgements

Authors would like to acknowledge the financial support from the National Natural Science Foundation of China (Nos. U1804146, 51801054 and 52111530068), Program for Science, Technology Innovation Talents in Universities of Henan Province (No.17HASTIT026), Foreign Experts and Introduction Project of Henan Province (HNGD2020009), as well as Science and Technology Innovation Team of Henan University of Science and Technology (No. 2015XTD006) as well as the Academy of Finland (No. 311934).

References

[1] E. Maawad, Y. Sano, L. Wangner, H.G. Brokmeier, C.H. Genzel, Investigation of laser shock peening effects on residual stress state and fatigue performance of titanium alloys, Mater. Sci. Eng. A 536 (2012) 82–91, https://doi.org/10.1016/jmsea.2011.12.072.

[2] X.L. Liu, C.Q. Sun, Y.S. Hong, Faceted crack initiation characteristics for high-cycle and very-high-cycle fatigue of a titanium alloy under different stress ratios, Int. J. Fatigue 92 (2016) 434–441, https://doi.org/10.1016/j.ijfatigue.2016.03.013.

[3] N. Ao, D.X. Liu, X.H. Zhang, K.F. Fan, H.L. Shi, Z. Liu, C.S. Liu, The effect of residual stress and gradient nanostructure on the fretting fatigue behavior of plasma electrolytic oxidation coated Ti–6Al–4V alloy, J. Alloys Compd. 811 (2019) 1–11, https://doi.org/10.1016/j.jallcom.2019.152017.

[4] Y.X. Chen, J.C. Wang, Y.K. Gao, A.H. Feng, Effect of shot peening on fatigue performance of Ti_2AlNb intermetallic alloy, Int. J. Fatigue 127 (2019) 53–57, https://doi.org/10.1016/j.ijfatigue.2019.05.034.

[5] X.F. Nie, W.F. He, S.L. Zang, X.D. Wang, J. Zhao, Effect study and application to improve high cycle fatigue resistance of TC11 titanium alloy by laser shock peening with multiple impacts, Surf. Coat. Technol. 253 (2014) 68–75, https://doi.org/10.1016/j.surfcoat.2014.05.015.

[6] S.H. Luo, L.C. Zhou, X.F. Nie, Y.H. Li, W.F. He, The compound process of laser shock peening and vibratory finishing and its effect on fatigue strength of Ti-3.5Mo-6.5Al-1.5Zr-0.25Si titanium alloy, J. Alloys Compd. 783 (2019) 828–835, https://doi.org/10.1016/j.jallcom.2018.12.294.

[7] S. Kumar, K. Chattopadhyay, V. Singh, Effect of ultrasonic shot peening on LCF behavior of the Ti–6Al–4V alloy, J. Alloys Compd. 724 (2017) 187–197, https://doi.org/10.1016/j.jallcom.2017.07.014.

[8] D.M. Ba, S.H. Ma, F.J. Meng, C.Q. Li, The investigation of surface nanocrystallization of structural steel induced by supersonic fine particles bombarding, Key Eng. Mater. 27 (2008) 811–814, https://doi.org/10.4028/www.scientific.net/KEM.373-374.811.
[9] K.Y. Luo, J.Z. Lu, L.F. Zhang, J.W. Zhong, H.B. Guan, X.M. Qian, The microstructural mechanism for mechanical property of LY2 aluminum alloy after laser shock processing, Mater. Des. 31 (5) (2009) 2599–2603, https://doi.org/10.1016/j.matdes.2009.11.026.
[10] L.Y. Kong, Y.X. Lao, T.Y. Xiong, T.F. Li, Nanocrystalline surface layer on AISI 52100 steel induced by supersonic fine particles bombarding, J. Therm. Spray Technol. 22 (6) (2013) 1007–1013, https://doi.org/10.1007/s11666-013-9934-7.
[11] M.L. Dong, X.F. Cui, B.W. Lu, X.R. Feng, S.Q. Song, G. Jin, H.D. Wang, Influence of surface nanocrystallization pretreatment on high-temperature vacuum carburizing behavior, J. Mater. Process. Technol. 278 (2020) 49–86, https://doi.org/10.1016/j.jmatprotec.2019.116519.
[12] H.M. Gao, W.G. Chen, Z.J. Zhang, Evolution mechanism of surface nano-crystallization of tungsten-copper alloys, Mater. Lett. 176 (2016) 181–184, https://doi.org/10.1016/j.matlet.2016.04.104.
[13] Y.X. Zhang, J.H. Yang, L.L. Ge, X. Zhang, J.Z. Chen, Research on mechanism of surface nanocrystalline layer in 2219 Al alloy induced by supersonic fine particles bombarding, Int. J. Eng. Res. Afr. 4438 (2016) 1–8, https://doi.org/10.4028/www.scientific.net/JERA.24.1.
[14] L.L. Ge, N. Tian, Z.X. Lu, C.Y. You, Influence of the surface nanocrystallization on the gas nitriding of Ti-6Al-4V alloy, Appl. Surf. Sci. 286 (2013) 412–416, https://doi.org/10.1016/j.apsusc.2013.09.105.
[15] L.L. Ge, Z.W. Yuan, X.T. Jing, Study of pure titanium (TA2) surface nanocrystallization and its thermal stablity, Rare Met. Eng. 40 (07) (2011) 1239-1242.
[16] Z.Q. Guo, L.L. Ge, H. Yuan, C. Qin, Surface nano-crystallization of TC4 titanium alloy and its thermal stability, Trans. Mater. Heat Treat. 33 (03) (2012) 114–118.
[17] B.S. Zhang, Q.S. Dong, Z.X. Ba, Z.Z. Wang, H.C. Shi, Y.T. Xue, Tribological properties of surface-textured and plasma-nitrided pure titanium under oil lubrication condition, J. Mater. Eng. Perform. 27 (1) (2018) 186–193, https://doi. org/10.1007/s11665-017-3100-1.
[18] M. Wang, Y. Fan, Electrochemical corrosion property of nanostructure layer of Ti-5Al-2Sn-2Zr-4Mo-4Cr titanium alloy, Int. J. Adv. Manuf. Technol. 96 (5–8) (2018) 1601–1606, https://doi.org/10.1007/s00170-017-0660-z.
[19] H. Su, X.H. Shen, C.H. Xu, J.Q. He, B.L. Wang, G.S. Su, Surface characteristics and corrosion behavior of TC11 titanium alloy strengthened by ultrasonic roller burnishing at room and medium temperature, J. Mater. Res. Technol. 9 (4) (2020) 8172–8185, https://doi.org/10.1016/j.jmrt.2020.05.059.
[20] T. Zhou, Y. Xiong, Z.C. Chen, X.Q. Zha, Y. Lu, T.T. He, F.Z. Ren, H.C. Singh, J. K. Komi, M.K. Huttula, W. Cao, Effect of surface nano-crystallization induced by supersonic fine particles bombarding on microstructure and mechanical properties of 300M steel, Surf. Coat. Technol. 421 (2021), 127381, https://doi.org/10.1016/j.surfcoat.2021.127381.
[21] Y.L. Wu, Y. Xiong, Z.G. Chen, X.Q. Zha, Y. Yue, Y.L. Liu, J.M. Zhang, F.Z. Ren, Effect of supersonic fine particle bombardment on microstructure and fatigue properties of TC11 titanium alloy, J. Mater. Eng. 49 (05) (2021) 137-143.
[22] C.S. Tan, Q.Y. Sun, G.J. Zhang, Y.Q. Zhao, Remarkable increase in high-cycle fatigue resistance in a titanium alloy with a fully lamellar microstructure, Int. J. Fatigue 138 (2020) 1–10, https://doi.org/10.1016/j.ijfatigue.2020.105724.
[23] M. Wen, G. Liu, J.F. Gu, W.M. Guan, J. Lu, Dislocation evolution in titanium during

surface severe plastic deformation, Appl. Surf. Sci. 255 (12) (2009) 6097–6102, https://doi.org/10.1016/j.apsusc.2009.01.048.
[24] P. Kumar, G.S. Mahobia, K. Chattopadhyay, Surface nanocrystallization of β-titanium alloy by ultrasonic shot peening, Mater. Today Proc. 28 (2) (2020) 486–490, https://doi.org/10.1016/j.matpr.2019.10.174.
[25] Z. Wang, J.G. Wang, Z.Y. Chen, M. Zha, C. Wang, S. Liu, R.F. Yan, Effect of Ce addition on modifying the microstructure and achieving a high elongation with a relatively high strength of as-extruded AZ80 magnesium alloy, Materials 12 (1) (2018) 1–12, https://doi.org/10.3390/ma12010076.
[26] K. Tokaji, High cycle fatigue behaviour of Ti–6Al–4V alloy at elevated temperatures, Scr. Mater. 54 (12) (2006) 2143–2148, https://doi.org/10.1016/j.matpr.2019.10.174.
[27] K. Lu, Making strong nanomaterials ductile with gradients, Science 345 (6203) (2014) 1455–1456, https://doi.org/10.1126/science.1255940.
[28] C.H. Liu, D.X. Liu, X.H. Zhang, D. Liu, A.M. Ma, N. Ao, X.C. Xu, Improving fatigue performance of Ti-6Al-4V alloy via ultrasonic surface rolling process, J. Mater. Sci. Technol. 35 (08) (2019) 1555–1562, https://doi.org/10.1016/j.jmst.2019.03.036.
[29] I. Altenberger, R.K. Nalla, Y.J. Sano, L. Wagner, R.O. Ritchie, On the effect of deep-rolling and laser-peening on the stress-controlled low- and high-cycle fatigue behavior of Ti-6Al-4V at elevated temperatures up to 550 °C, Int. J. Fatigue 44 (2012) 292–302, https://doi.org/10.1016/j.ijfatigue.2012.03.008.
[30] Y.N. Chen, Y. Xiong, M.X. Fan, Y. Yue, H. Yao, F.Z. Ren, Fatigue fracture analysis of TC11 titanium alloy at different temperatures, Trans. Mater. Heat Treat. 40 (8) (2019) 61-68.
[31] R.J. Sun, L.H. Li, Y. Zhu, P. Peng, Q. Li, W. Guo, Fatigue of Ti-17 titanium alloy with hole drilled prior and post to laser shock peening, Opt. Laser Technol. 115 (2019) 166–170, https://doi.org/10.1016/j.optlastec.2019.02.019.
[32] T. Zhou, Y. Xiong, Y. Yue, Y. Lu, Y.N. Chen, T.T. He, F.Z. Ren, H. Singh, J. Komi, M. Huttula, W. Cao, Controlled cold rolling effect on microstructure and mechanical properties of Ce-modified SAF 2507 super duplex stainless steel, Mater. Sci. Eng. A 766 (2019), 138352, https://doi.org/10.1016/j.msea.2019.138352.
[33] H. Lee, S. Mall, Stress relaxation behavior of shot-peened Ti-6Al-4V under fretting fatigue at elevated temperature, Mater. Sci. Eng. A 366 (2) (2003) 412–420, https://doi.org/10.1016/j.msea.2003.09.064.
[34] Y.G. Liu, M.Q. Li, H.J. Liu, Surface nanocrystallization and gradient structure developed in the bulk TC4 alloy processed by shot peening, J. Alloys Compd. 685 (2016) 186–193, https://doi.org/10.1016/j.jallcom.2016.05.295.
[35] D. Liu, D.X. Liu, X.H. Zhang, C.S. Liu, N. Ao, Surface nanocrystallization of 17-4 precipitation-hardening stainless steel subjected to ultrasonic surface rolling process, Mater. Sci. Eng. A 726 (2018) 69–81, https://doi.org/10.1016/j.msea.2018.04.033.
[36] H.W. Huang, Z.B. Wang, J. Lu, K. Lu, Fatigue behaviors of AISI 316L stainless steel with a gradient nanostructured surface layer, Acta Mater. 87 (2015) 150–160, https://doi.org/10.1016/j.actamat.2014.12.057.
[37] J.R. Luo, X. Song, L.Z. Zhuang, J.S. Zhang, Twinning behavior of a basal textured commercially pure titanium alloy TA2 at ambient and cryogenic temperatures, J. Iron Steel Res. Int. 23 (1) (2016) 74–77, https://doi.org/10.1016/S1006-706X(16)30015-2.
[38] B.K. Zhao, P. Huang, L.B. Zhang, S.Z. Li, Z. Zhang, Q. Yu, Temperature effect on stacking fault energy and deformation mechanisms in titanium and titanium-aluminium alloy, Sci. Rep. 10 (1)

(2020) 3086, https://doi.org/10.1038/s41598-020-60013-6.
[39] Y. Huang, J.Z. Zhou, J. Li, X.L. Tian, X.K. Meng, S. Huang, Effects of cryogenic laser peening on damping characteristics and vibration fatigue life of TC6 titanium, Chin. J. Lasers 47 (04) (2020) 149-156.
[40] Y. Ren, F.C. Wang, C.W. Tan, S.Y. Wang, X.D. Yu, J.W. Jiang, H.N. Cai, Effect of shock-induced martensite transformation on the postshock mechanical response of metastable β titanium alloys, J. Alloys Compd. 578 (2013) 547–552, https://doi.org/10.1016/j.jallcom.2013.07.028.
[41] D.L. Ouyang, S.Q. Lu, X. Cui, X. Li, X. Huang, Transformation of deformation-induced martensite in TB6 titanium alloy, Chin. J. Nonferrous Met. 20 (12) (2010) 2307-2312.
[42] L.Q. Wang, Q.Q. Wei, W.J. Lu, J.N. Tan, F. Zhang, D. Zhang, Martensite phase transformation of TiNbTaZr alloy during cold rolling, Chin. J. Nonferrous Met. 20 (10) (2010) 473-477.
[43] Q.Y. Sun, S.J. Song, R.H. Zhu, H.C. Gu, Toughening of titanium alloys by twinning and martensite transformation, J. Mater. Sci. 37 (12) (2002) 2543–2547, https://doi.org/10.1023/A:1015456026919.